ELSEVIER

A semi-analytical finite element formulation for modeling stress wave propagation in axisymmetric damped waveguides

Alessandro Marzani[a],[*], Erasmo Viola[a], Ivan Bartoli[b],
Francesco Lanza di Scalea[b], Piervincenzo Rizzo[c]

[a]*Dipartimento di Ingegneria delle Strutture, dei Trasporti, delle Acque, del Rilevamento, del Territorio (DISTART),
Università degli Studi di Bologna, Via Risorgimento 2, 40136 Bologna, Italy*
[b]*NDE & Structural Health Monitoring Laboratory, Department of Structural Engineering, University of California,
San Diego, 9500 Gilman Drive, La Jolla, CA 92093-0085, USA*
[c]*Department of Civil & Environmental Engineering, University of Pittsburgh, 949 Benedum Hall,
3700 O'Hara Street, Pittsburgh, PA 15261, USA*

Abstract

A semi-analytical finite element (SAFE) method is presented for analyzing the wave propagation in viscoelastic axisymmetric waveguides. The approach extends a recent study presented by the authors, in which the general SAFE method was extended to account for material damping. The formulation presented in this paper uses the cylindrical coordinates to reduce the finite element discretization over the waveguide cross-section to a mono-dimensional mesh. The algorithm is validated by comparing the dispersion results with viscoelastic cases for which a Superposition of Partial Bulk Waves solution is known. The formulation accurately predicts dispersion properties and does not show any missing root. Applications to viscoelastic axisymmetric waveguides with varying mechanical and geometrical properties are presented.
© 2008 Elsevier Ltd. All rights reserved.

1. Introduction

Guided ultrasonic waves (GUWs) provide a highly efficient method for the non-destructive evaluation (NDE) and the structural health monitoring (SHM) of waveguides such as beam-like or plate-like structures. Compared to ultrasonic bulk waves, the use of GUWs provides: (a) longer inspection range, (b) larger versatility owing to dispersive and multimodal nature and (c) complete coverage of the waveguide cross-section. These advantages can be fully exploited only once the complexities of guided wave propagation are unveiled and managed for the given test structure.

These complexities include the existence of multiple modes that can propagate simultaneously, and the frequency-dependent velocities and attenuation (dispersive behavior). For example, the knowledge of the wave

*Corresponding author. Tel.: +39 051 2093504; fax: +39 051 2093594.
E-mail address: alessandro.marzani@mail.ing.unibo.it (A. Marzani).

velocity is important for mode identification. Similarly, the knowledge of those mode–frequency combinations propagating with minimum attenuation losses helps maximizing the inspection coverage.

To date, among others, Superposition of Partial Bulk Waves (SPBW) and Semi-Analytical Finite Element (SAFE) methods are the most efficient tools for modeling GUWs propagation. SPBW methods are well-established analytical algorithms in which the wave equation is formulated via constructive interference of partial bulk waves with respect to the waveguide boundary conditions. For damped and/or leaky waves solutions are usually obtained by searching for those combinations of frequency and complex wavenumber that satisfy the wave equation. Minimum searching routines that rely on the slope [1] or on the local minima [2] of the wave equation characteristic function are generally used. A comprehensive literature review on SPBW methods in cylindrical and plate-like systems can be found in Refs. [3] and [2], respectively.

In SAFE methods, finite elements over the waveguide cross-section are coupled to harmonic functions along the wave propagation direction to describe the wave displacement field. The application of a variational scheme, leads the governing wave equation to be defined by a system of algebraic equations having the frequency and wavenumber as unknowns. Guided wave solutions are then obtained by using standard routines for eigenvalue problems.

The groundwork for the SAFE method is attributed to Nelson, Dong and co-authors [4,5] that successfully formulated the SAFE wave equations for elastic layered orthotropic cylinders and plates by means of a mono-dimensional cross-section interpolation.

Two years later, Aalami [6], introducing a bi-dimensional discretization, extended the technique formulating the wave equation for a square rod and demonstrated that the SAFE method was applicable to waveguides of arbitrary cross-section.

Afterwards, the SAFE method has been effectively used to model guided wave propagation in anisotropic composite cylinders [7–9], laminated composite plates [10–12], wedges [13], rails [14,15], functionally graded cylinders [16], piezoelectric plates [17], laminated piezoelectric cylinders [18] and channel beams [19].

The focus of these works was the characterization of the propagative and evanescent guided modes in waveguides with neither material damping nor energy leakage, i.e. without attenuation. Due to great importance of attenuation on GUWs propagation a need to extend the SAFE approach to waveguides with material damping exists.

A common approach to introduce damping is to account for hysteresis by considering the viscous properties of materials. Shorter [20], for example, presented a SAFE formulation capable to calculate the damping loss factor of propagative guided modes in laminates by considering linear viscoelastic materials.

More recently, Bartoli et al. [21] proposed a SAFE scheme that, accounting for linear viscoelastic materials, is capable of extracting GUWs dispersive features, such attenuation and energy velocity, in damped waveguides. The algorithm in Ref. [21] has been validated by comparing the results with several SPBW solutions found in literature [22–25] and it has been successfully used to model GUWs propagation in hysteretic composite joints [26,27].

The present study expands the SAFE formulation in Ref. [21] by exploiting cylindrical coordinates. For axisymmetric waveguides, such extension allows to reduce the bi-dimensional discretization to a single radial line of mono-dimensional elements, improving the algorithm efficiency and accuracy. The SAFE results have been compared to SPBW solutions for an elastic copper tube filled with viscoelastic bitumen and for a steel pipe coated by a thin layer of viscoelastic bitumen. Dispersion results are also presented for a viscoelastic three-layer system consisting in a steel strand embedded in grout and concrete. To the authors' knowledge, no work has been published on the SAFE formulation of axisymmetric waveguides with viscoelastic losses.

2. SAFE damped wave equation

2.1. Problem statement

Let us consider an infinitely long, axisymmetric waveguide immersed in vacuum with the cross-section laying in the r–θ plane, as shown in Fig. 1(a). In the most general case, the waveguide is composed of several anisotropic viscoelastic axisymmetric layers, with constant material properties along the axial z-direction.
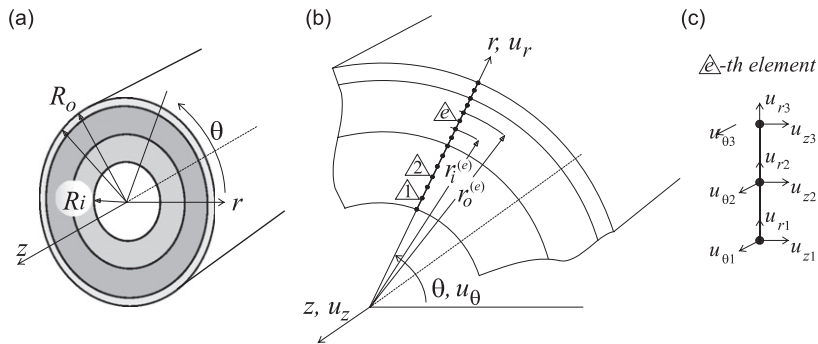
Fig. 1. (a) Schematic representation of a multilayered hollow cylinder, (b) representation of the through-thickness mono-dimensional finite element mesh, (c) *e*th mono-dimensional quadratic finite element with three degrees of freedom per node.

For an harmonic wave propagating along the axial direction, the displacement $\mathbf{u}(\mathbf{x}, t) = [u_r \, u_\theta \, u_z]^{\mathrm{T}}$, strain $\boldsymbol{\varepsilon}(\mathbf{x}, t) = [\varepsilon_{rr} \, \varepsilon_{\theta\theta} \, \varepsilon_{zz} \, \varepsilon_{\theta z} \, \varepsilon_{rz} \, \varepsilon_{r\theta}]^{\mathrm{T}}$ and stress $\boldsymbol{\sigma}(\mathbf{x}, t) = [\sigma_{rr} \, \sigma_{\theta\theta} \, \sigma_{zz} \, \sigma_{\theta z} \, \sigma_{rz} \, \sigma_{r\theta}]^{\mathrm{T}}$ complex vectors at a point $\mathbf{x} \equiv (r, \theta, z)$ and time t can be described as:

$$\mathbf{u} = \mathbf{A}(r)\mathrm{e}^{\mathrm{i}(n\theta + \xi z - \omega t)}, \quad \boldsymbol{\varepsilon} = \mathbf{L}\mathbf{u}, \quad \boldsymbol{\sigma} = \tilde{\mathbf{C}}\boldsymbol{\varepsilon} \tag{1}$$

where $\mathbf{A}(r) = [A_r \, A_\theta \, A_z]^{\mathrm{T}}$ is the 3×1 polarized amplitude vector, n is the circumferential order number, ξ is the axial wavenumber, ω is the wave circular frequency and the superscript T represents a transpose vector. In Eq. (1) $\mathbf{L}$ is the compatibility operator in cylindrical coordinates for infinitesimal strain and $\tilde{\mathbf{C}}$ is complex constitutive matrix that describes the viscoelastic properties of the material [28].

2.2. Axisymmetric SAFE formulation

A finite element mono-dimensional mesh through the thickness of the waveguide (see Fig. 1(b)) is adopted to approximate the displacement $\mathbf{u}$ as $\mathbf{u}_h = \mathbf{N}\mathbf{q}\mathrm{e}^{\mathrm{i}(n\theta + \xi z - \omega t)}$, where $\mathbf{N}$ is the matrix of the shape functions and $\mathbf{q}$ is the vector of nodal displacements. Assuming an isentropic condition, where heat conduction is neglected and energy dissipative processes are much less important than processes which conserve energy, the application of the Hamilton's variational principle leads to [20]:

$$\bigcup_{e=1}^{n_{\mathrm{el}}} \left\{ \int_{-\infty}^{+\infty} \int_0^{2\pi} \int_{r_i^{(e)}}^{r_o^{(e)}} [\delta(\mathbf{L}\mathbf{u}_h)^{\mathrm{T}} \tilde{\mathbf{C}}^{(e)} \mathbf{L}\mathbf{u}_h - \omega^2 \delta(\mathbf{u}_h)^{\mathrm{T}} \rho^{(e)} \mathbf{u}_h] r \, \mathrm{d}r \, \mathrm{d}\theta \, \mathrm{d}z \right\} = 0 \tag{2}$$

where n_{el} is the total number of elements in the mesh, $\rho^{(e)}$ and $\tilde{\mathbf{C}}^{(e)}$ are the mass density and the complex constitutive matrix of the *e*th element delimited by the inner and outer radius $r_i^{(e)}$ and $r_o^{(e)}$, as indicated in Fig. 1(b). Common algebra and standard finite element assembling procedure leads to:

$$[\mathbf{A}(n, \omega) - \xi\mathbf{B}(n, \omega)]_{2M}\mathbf{U} = \mathbf{0} \tag{3}$$

where $\mathbf{U}$ is the global vector of nodal displacements and the subscript $2M$ indicates the equation dimension. The equations given in Ref. [29] for the calculation of the matrices $\mathbf{A}$ and $\mathbf{B}$ for undamped media still hold when material damping is included. However, in this case, these matrices result to be complex as a result of the complex stiffness matrices $\tilde{\mathbf{C}}$. Eq. (3) is the final wave equation for damped waveguides that for a given order mode n can be solved for each input frequency, once the complex stiffness matrices for the materials at that frequency are known [21].

2.3. Remarks on the complex stiffness matrix

Herein an hysteretic (structural) frequency independent rheological model is assumed [30–32]. For isotropic materials, the coefficients $\tilde{C}_{ij}$ of the complex stiffness matrix depend only on the two complex Lamè moduli,

$\tilde{\mu} = \rho \tilde{c}_S^2$ and $\tilde{\lambda} = \rho[\tilde{c}_L^2 - 2\tilde{c}_S^2]$, that can be calculated by means of the following constants [31,32]:

$$\tilde{c}_{L,S} = c_{L,S}\left(1 + \mathrm{i}\frac{\kappa_{L,S}}{2\pi}\right)^{-1} \tag{4}$$

where $c_{L,S}$ $(\mathrm{m\,s^{-1}})$ and $\kappa_{L,S}$ $(\mathrm{Np}\,\lambda^{-1})$ are the material longitudinal and shear bulk wave speeds and attenuations, respectively.

This rheological model, often assumed in literature due to its straightforward implementation, can accurately represent the behavior of a limited number of materials and its precision is restricted to finite frequency ranges. However, this rheological model was employed to demonstrate the reliability of the SAFE formulation in the calculation of the dispersive attenuation curves for axially symmetric waveguides. It should be noted that, as previously discussed by the authors in Ref. [21], the SAFE method can be extended to different rheological models as the Kelvin–Voigt model where the attenuation of bulk waves is frequency dependent.

Future work will consider the extension of this SAFE formulation to others rheological models, such as the linear standard solid model, already implemented in analytically based formulation for plate waves [33].

3. Guided wave features

For viscoelastic materials solving Eq. (3) for a given input frequency ω yields $m = 1$–$2M$ complex eigenvalues $\xi^m = \xi_{\mathrm{Re}}^m + \mathrm{i}\xi_{\mathrm{Im}}^m$ and the corresponding eigenvectors $\mathbf{U}^m = \mathbf{U}_{\mathrm{Re}}^m + \mathrm{i}\mathbf{U}_{\mathrm{Im}}^m$. Only half of the $2M$ roots of the dispersion relation are independent (ξ^m). The remaining M solutions are defined as $-\bar{\xi}^m$, where the overbar means complex conjugate.

From the mth eigenvalue ξ^m the phase velocity $c_{ph}^m = \omega/\xi_{\mathrm{Re}}^m$ $(\mathrm{m\,s^{-1}})$ and the attenuation $\mathrm{att}^m = \xi_{\mathrm{Im}}^m$ $(\mathrm{Np\,m^{-1}})$ for the mth guided mode are obtained. From the corresponding eigenvector $\mathbf{U}^m$, instead, the nodal displacement vector $\mathbf{q}^m$ for each finite element in the mesh ($e = 1$–n_{el}) can be extracted and the displacement $\mathbf{u}_h^m$, strain $\boldsymbol{\varepsilon}_h^m$ and stress $\boldsymbol{\sigma}_h^m$ at a point reconstructed. The time averaged strain and kinetic energy densities at a point are then obtained as:

$$\langle \mathrm{S}^m \rangle_T = \frac{1}{4}\mathrm{Re}[(\boldsymbol{\sigma}_h^m)^{\mathrm{T}} \bar{\boldsymbol{\varepsilon}}_h^m] \quad (\mathrm{J\,m^{-3}}) \tag{5}$$

$$\langle \mathrm{K}^m \rangle_T = \frac{1}{4}\rho(\dot{\mathbf{u}}_h^m)^{\mathrm{T}} \bar{\dot{\mathbf{u}}}_h^m \quad (\mathrm{J\,m^{-3}}) \tag{6}$$

where $\langle \cdots \rangle_T = (1/T)\int_0^T (\cdots)\,\mathrm{d}t$ is the time-averaging operator and $T = 2\pi/\omega$ is the period [36]. For the mth mode, the power flow density vector at a given point, also known as the Poynting vector, can be obtained by time-averaging over a unit period the product of the stress tensor and the velocity vector:

$$\langle \mathbf{P}^m \rangle_T = \begin{bmatrix} P_r^m & P_\theta^m & P_z^m \end{bmatrix}^{\mathrm{T}} = -\frac{1}{2}\mathrm{Re}\left(\tilde{\boldsymbol{\sigma}}_h^m \bar{\mathbf{u}}_h^m\right) \quad (\mathrm{J\,s^{-1}m^{-2}}) \tag{7}$$

where $\tilde{\boldsymbol{\sigma}}_h^m$ is the conventional 3×3 stress tensor [37].

The representation of the Poynting vector over the waveguide cross-section is useful to show how the energy is flowing in the structure, for example the depth at which the greatest transmission of energy takes place, or the manner in which energy transmits from one layer to the adjacent one. Note that for GUWs propagating in the z-direction, the Poynting vector component in the circumferential direction is zero, $P_\theta^m = 0$. In addition, if there is no leakage or damping, also the component in the radial direction is zero, $P_r^m = 0$, i.e. the power flow is entirely in the direction of the wave propagation [35].

The rate at which mth mode energy is transmitted along the structure is indicated by the mode power flow, PF^m, which can be obtained by integrating over the waveguide cross-section Ω the component of the Poynting vector in the propagation direction [38]:

$$PF^m = \int_\Omega (\mathbf{P}^m \cdot \hat{z})\,\mathrm{d}\Omega = 2\pi \int_{R_i}^{R_o} P_z^m r\,\mathrm{d}r \quad (\mathrm{J\,s^{-1}}) \tag{8}$$

The wave energy velocity for the *m*th mode, V_e^m, can be finally obtained as the ratio of the mode power flow and the total energy density (kinetic and strain) for the whole cross-section:

$$V_e^m = PF^m \left\{ 2\pi \int_{R_i}^{R_o} [\langle \mathbf{S}^m \rangle_T + \langle \mathbf{K}^m \rangle_T] r \, \mathrm{d}r \right\}^{-1} \quad (\mathrm{m\,s^{-1}}) \tag{9}$$

Since quadratic mono-dimensional elements were adopted in the formulation (see Fig. 1(c)), an exact three point Gaussian integration was used in Eqs. (8) and (9) to perform the spatial integration through the thickness of the waveguide.

4. Numerical validation of the SAFE formulation

For the purpose of validating the accuracy of the proposed formulation, the SAFE cut-off frequencies f_{cut}^m of a scheduled 4-in ANSI 40 steel pipe were compared with those calculated with a SPBW algorithm [39].

Since cut-off frequencies do not have meaning in damped waveguides, material damping was not considered. Geometrical and material properties of the pipe are defined in Table 1. For several refined meshes ($n_{\mathrm{el}} = 1,2,4,8,16,32$) the SAFE cut-off frequencies were calculated for a given circumferential wavenumber n assuming $\xi = 0$. The SPBW cut-off frequencies were calculated with a zero finding routine based on the Ridder's method considering a maximum frequency tolerance of 1×10^{-5} Hz. In Table 2 the SAFE and SPBW cut-off frequencies for the co-existing torsional $T(0, j)$, longitudinal $L(0, j)$ and first-order flexural modes $F(1, j)$, are given in the 0–1000 kHz frequency range.

Torsional modes were analyzed considering only the dof in the ϑ-direction. Complementarily, the $r-z$ dof were used to describe the longitudinal modes. Therefore, for a mesh with one quadratic finite element ($n_{\mathrm{el}} = 1$) only 3 dof were available to extract the pure torsional modes and the $T(0,4)$ could not be calculated. Likewise, for $n_{\mathrm{el}} = 1$, the longitudinal $L(0,7)$, flexural $F(1,10)$ and $F(1,11)$ modes were not found. As expected, SAFE slightly overestimates the cut-off frequencies because discretized systems are stiffer than real structures, producing higher natural frequencies. However, by increasing the number of finite elements, the SAFE solution converges rapidly to the SPBW one.

Table 1
Waveguides geometrical and acoustic material properties

Case	Material	Inner radius R_i (mm)	Outer radius R_o (mm)	Density ρ (kg m^{-3})	Long. bulk speed c_L (m s^{-1})	Shear bulk speed c_T (m s^{-1})	Long. bulk attenuation κ_L (Np λ^{-1})	Shear bulk attenuation κ_T (Np λ^{-1})
5.1	TML 24515 45/60 bitumen core[a]	0	6.8	970	–	430	–	1.350
	Elastic copper pipe[a]	6.8	7.5	8900	–	2240	–	0
5.2	Elastic 4-in 40 ANSI steel pipe[b]	51.181	57.150	7800	5900	3190	0	0
	Viscoelastic bitumen coating[b]	57.150	57.3024	1500	1860	750	0.2688	1.131
5.3	Elastic steel strand[c]	0	7.62	7932	5960	3260	0.003	0.008
	Viscoelastic grout[c]	7.62	31.75	1600	2810	1700	0.043	0.100
	Viscoelastic concrete[d]	31.75	76.20	2152	3758	2090	0.186	0.229

[a]Acoustic properties from Ref. [34].
[b]Acoustic properties obtained by those in Ref. [32].
[c]Acoustic properties from Ref. [25].
[d]Acoustic properties from Ref. [41].

Table 2
Cut-off frequencies for a 4 in. 40 ANSI steel pipe in the range 0–1000 kHz for an increasing number of finite elements n_{el} used in the SAFE mesh

Guided mode	Cut-off frequencies (kHz)						SPBW solution
	SAFE number of finite elements						
	$n_{el} = 1$	$n_{el} = 2$	$n_{el} = 4$	$n_{el} = 8$	$n_{el} = 16$	$n_{el} = 32$	
$T(0,2)$	295.3614	268.8374	267.8991	267.8348	267.8307	267.8306	267.8304
$T(0,3)$	659.2486	589.6497	536.7450	534.8738	534.7456	534.7373	534.7368
$T(0,4)$	no data	965.2810	815.0922	802.8491	801.9137	801.8511	801.8479
$L(0,2)$	15.7913	15.7913	15.7913	15.7912	15.7913	15.7533	15.7913
$L(0,3)$	294.7276	268.3422	267.4058	267.3417	267.3376	267.3374	267.3374
$L(0,4)$	544.9717	496.3560	494.6273	494.5090	494.5014	494.4992	494.5009
$L(0,5)$	658.9309	589.3322	536.4968	534.6265	534.4984	534.4902	534.4897
$L(0,6)$	1218.7344	964.9626	814.9279	802.6840	801.7489	801.6872	801.8630
$L(0,7)$	no data	1089.9189	992.2911	988.8335	988.5967	988.5805	988.5805
$F(1,2)$	9.3779	9.3779	9.3779	9.3779	9.3783	9.3708	9.3779
$F(1,3)$	22.2642	22.2641	22.2641	22.2642	22.2651	22.2590	22.2641
$F(1,4)$	294.8777	268.5068	267.5711	267.5070	267.5029	267.5025	267.5026
$F(1,5)$	295.9331	269.4079	268.4678	268.4033	268.3992	268.3987	268.3990
$F(1,6)$	544.8441	496.0422	493.9608	493.8121	493.8024	493.7999	493.8018
$F(1,7)$	658.9978	589.4070	536.5790	534.7090	534.5809	534.5725	534.5722
$F(1,8)$	659.6892	590.2145	537.6638	535.8220	535.6958	535.6870	535.6871
$F(1,9)$	1218.7931	965.0083	814.9812	802.7389	801.8038	801.7420	801.7380
$F(1,10)$	no data	965.2204	815.0712	802.8292	801.8941	801.8311	801.8283
$F(1,11)$	no data	1090.1726	992.4761	989.0179	988.7802	988.7638	988.7639

Analytical solution is obtained by a SPBW formulation from Ref. [39].

For the same waveguide, a second accuracy test was performed by comparing the axial wavenumbers at the frequency of 1 MHz. The SAFE wavenumbers were obtained for different meshes by solving Eq. (3) at the desired frequency. For the SPBW algorithm a maximum frequency tolerance of 1×10^{-5} Hz and a maximum phase speed tolerance of 1×10^{-5} m s^{-1} were used in the roots searching routine. Results are summarized in Table 3.

It can be seen in this case that the SAFE formulation underestimates the wavenumbers. In fact, in discretized (stiffer) structures, guided modes propagate with higher phase speed, i.e. lower wavenumber. Again, with increasing number of elements in the mesh, the SAFE wavenumbers converge rapidly to the SPBW solutions.

The results presented in Tables 2 and 3 confirm that the SAFE meshing criteria proposed by Galan and Abascal [40] for homogeneous plate-like waveguides is also valid for the case of axis symmetric homogeneous waveguides. This criterion guarantees SAFE solution accuracy by adopting finite elements of maximum dimension $L_{max} = \lambda_T/\beta$, where $\lambda_T = 2\pi c_T/\omega_{max}$, $\beta = 4$ for quadratic finite elements and $\omega_{max} = 2\pi f_{max}$ is the highest circular frequency for which the solution is sought. In this example, where $c_T = 3190$ m/s and $f_{max} = 1$ MHz, the maximum element length is $L_{max} = 0.7975$ mm. Therefore, for the system under study (wall-thickness $R_o - R_i = 5.969$ mm) the above criteria is satisfied by considering a minimum of eight finite elements in the mesh.

It can be observed in Table 2 that for $n_{el} = 8$, the maximum error on the cut-off frequencies is around 0.12% for the modes $T(0,4)$, $F(1,9)$ and $F(1,10)$ while the maximum error on the wavenumbers, reported in Table 3, is around 1.4% for the longitudinal $L(0,7)$ and flexural $F(1,11)$ mode. The correctness of the formulation was also verified proving that the boundary conditions for cross-sectional distribution of multiple guided wave features (displacements, Poynting vector components, energy velocity, etc.) were respected.

Table 3
Guided modes wavenumbers for a 4 in. 40 ANSI steel pipe at 1 MHz for increasing number of finite elements n_{el} used in the SAFE mesh

Modes @ 1000 kHz	Wavenumber (m^{-1})						SPBW solution
	SAFE number of finite elements						
	$n_{el} = 1$	$n_{el} = 2$	$n_{el} = 4$	$n_{el} = 8$	$n_{el} = 16$	$n_{el} = 32$	
$T(0,1)$	1969.6505	1969.6505	1969.6505	1969.6505	1969.6506	1969.6502	1969.6506
$T(0,2)$	1881.7758	1897.1390	1897.6538	1897.6891	1897.6913	1897.6913	1897.6915
$T(0,3)$	1481.0296	1590.8062	1661.8818	1664.2207	1664.3805	1664.3909	1664.3915
$T(0,4)$	no data	514.4999	1141.0802	1174.2706	1176.7477	1176.9131	1176.9218
$L(0,1)$	2012.4827	2056.8344	2110.6264	2132.4272	2135.4840	2135.7271	2135.7426
$L(0,2)$	1901.4722	2023.9905	2085.9396	2110.1576	2113.4772	2113.7391	2113.7561
$L(0,3)$	1184.9864	1507.0610	1706.5366	1715.5892	1716.2380	1716.2822	1716.2832
$L(0,4)$	1030.3750	1123.8164	1205.9364	1230.2622	1232.3134	1232.4523	1232.4598
$L(0,5)$	719.0069	843.4473	977.7119	998.4361	1000.0818	1000.1917	1000.1992
$L(0,6)$	no data	659.1574	958.2004	973.1884	974.4192	974.5025	974.5074
$L(0,7)$	no data	no data	120.4295	145.7714	147.7086	147.8419	147.8439
$F(1,1)$	2012.3988	2056.7524	2110.5467	2132.3483	2135.4052	2135.6484	2135.6638
$F(1,2)$	1969.5636	2023.9054	2085.8566	2110.0754	2113.3952	2113.6572	2113.6741
$F(1,3)$	1901.3838	1969.5640	1969.5641	1969.5641	1969.5641	1969.5642	1969.5641
$F(1,4)$	1881.6825	1897.0482	1897.5631	1897.5984	1897.6006	1897.6010	1897.6008
$F(1,5)$	1480.9147	1590.6996	1706.4379	1715.4908	1716.1396	1716.1841	1716.1849
$F(1,6)$	1184.8409	1506.9465	1661.7775	1664.1167	1664.2765	1664.2878	1664.2875
$F(1,7)$	1030.2084	1123.6643	1205.7965	1230.1255	1232.1769	1232.3159	1232.3233
$F(1,8)$	718.7688	843.2457	1140.9286	1174.1227	1176.6001	1176.7667	1176.7742
$F(1,9)$	no data	658.8970	977.5362	998.2641	999.9101	1000.0202	1000.0276
$F(1,10)$	no data	514.1672	958.0220	973.0130	974.2440	974.3275	974.3321
$F(1,11)$	no data	no data	119.0030	144.5963	146.5492	146.6842	146.6856

Analytical solution is obtained by a SPBW formulation from Ref. [39].

5. Numerical applications

5.1. Elastic copper tube filled with elastic and viscoelastic bitumen

The first example examines an isotropic elastic copper pipe filled with viscoelastic TML 24515 45/60 bitumen. Wave propagation analysis in this system was performed by a SPBW formulation in Ref. [34]. In this paper, Simonetti and Cawley [34] proposed an NDE technique to estimate the bulk properties of the viscoelastic core by measuring the speed and attenuation of the fundamental Torsional guided mode. In the 0–150 kHz frequency range the bitumen was found behaving as a hysteretic media with constant complex shear moduli $\tilde{\mu} = \rho \tilde{c}_S^2$. Geometrical and material properties are given in Table 1.

For the SAFE calculation, the elastic stiffness tensor $\mathbf{C}$ for the copper and the constant complex stiffness matrix $\tilde{\mathbf{C}}$ for the bitumen were obtained as indicated in Section 2.3. Since the longitudinal bulk properties do not have an effect on the $T(0,j)$ modes for this system were arbitrarily assumed equal to zero.

For a maximum frequency $f_{max} = 150$ kHz, eleven quadratic elements, ten in the core and one in the pipe, were used to satisfy the mesh criteria proposed in Ref. [40].

Torsional modes were analyzed by considering only the 23 u_θ dof over the total $[n_{el} \times (n_n - 1) + 1] \times n_{dof} = 69$ dof, where $n_n = 3$ is the number of nodes per element and $n_{dof} = 3$ is the number of dof per node, i.e. u_r, u_θ and u_z.

SAFE results for the Torsional modes are shown in Fig. 2. On the left column the phase velocity (a), energy velocity (b) and attenuation (c) dispersion curves are given assuming the bitumen core as an elastic media neglecting the bulk shear wave attenuation (undamped system). The same dispersive features are presented on the right column considering the bitumen core as a viscoelastic material (damped system). In all these plots,
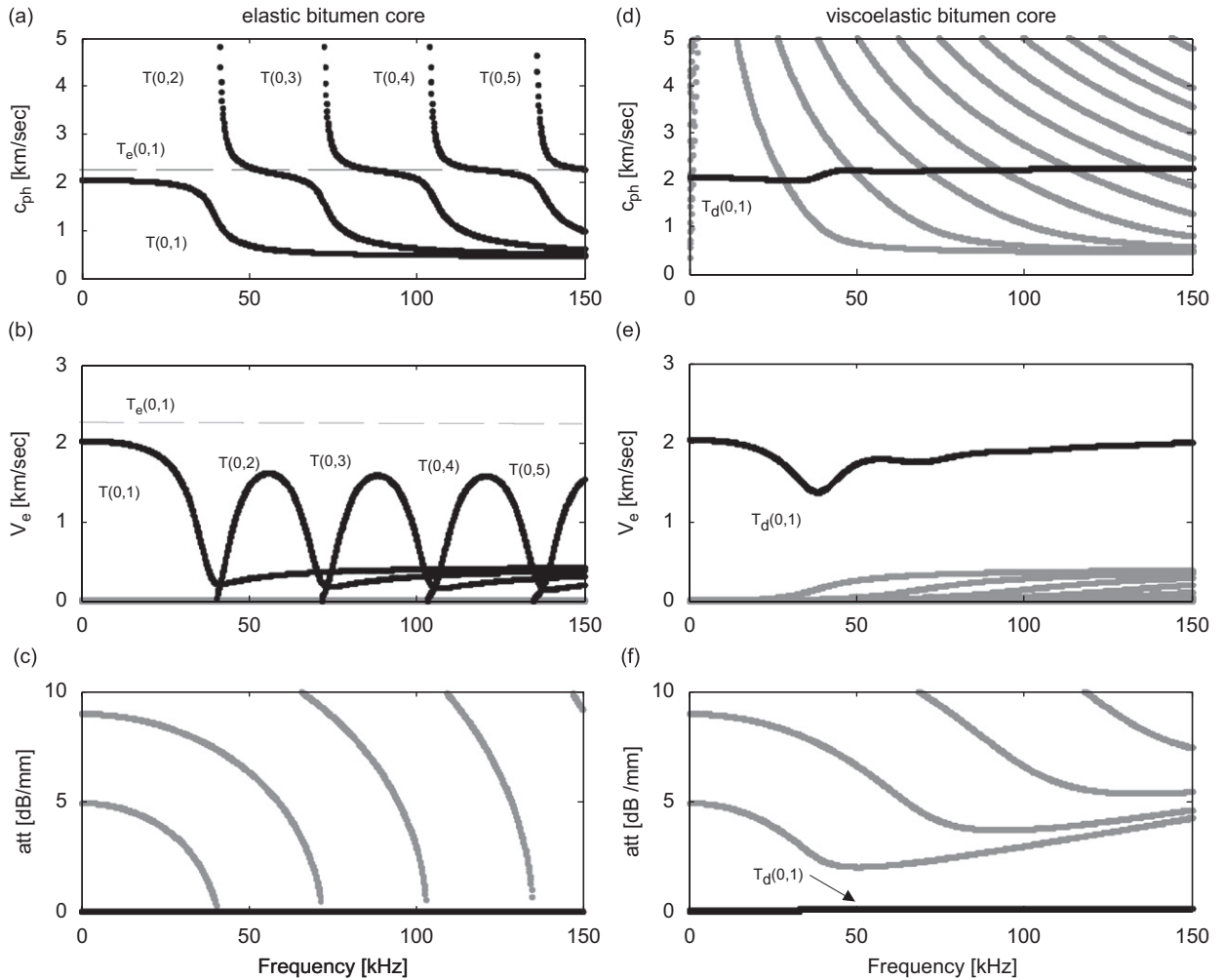
Fig. 2. Torsional modes for a copper ($\rho = 8900\,\mathrm{kg\,m^{-3}}$, $c_T = 2240\,\mathrm{m\,s^{-1}}$, $\kappa_T = 0\,\mathrm{Np}\,\lambda^{-1}$) pipe with inner radius 6.80 mm and wall thickness 0.70 mm, filled with bitumen. (a) Phase velocity, (b) energy velocity and (c) attenuation results considering the bitumen as an elastic medium ($\rho = 970\,\mathrm{kg\,m^{-3}}$, $c_T = 430\,\mathrm{m\,s^{-1}}$, $\kappa_T = 0\,\mathrm{Np}\,\lambda^{-1}$). (d) Phase velocity, (e) energy velocity and (f) attenuation considering the bitumen as a viscoelastic medium ($\rho = 970\,\mathrm{kg\,m^{-3}}$, $c_T = 430\,\mathrm{m\,s^{-1}}$, $\kappa_T = 1.35\,\mathrm{Np}\,\lambda^{-1}$). The dashed line in (a) and (b) correspond to the non-dispersive fundamental Torsional mode for the empty copper pipe $T_e(0,1)$.

roots with att $> 130\,\mathrm{dB\,m^{-1}}$ were marked with a brighter color. The dashed line in Fig. 2(a) and (b) indicates the non-dispersive fundamental Torsional mode for the empty copper pipe $T_e(0,1)$.

For the undamped system, among the 23 possible independent roots at each frequency the number of propagative (real wavenumber) modes vary from one, at near zero frequency, to five, at 150 kHz (see Fig. 2(a)). The remaining roots represent the evanescent modes (imaginary wavenumber). In Fig. 2(c), only the evanescent modes with att $< 10\,\mathrm{dB\,mm^{-1}}$ are shown.

The fundamental $T(0,1)$ mode starts propagating at around $2030.2\,\mathrm{m\,s^{-1}}$ phase speed, it behaves as non-dispersive up to 30 kHz and for increasing frequency its velocity drops down to the shear bulk wave speed of the bitumen. As it can be seen from Fig. 2(b), the higher order Torsional modes, i.e. $T(0,2)$, $T(0,3)$, $T(0,4)$ and $T(0,5)$, start propagating at their cut-off frequencies $f_{\mathrm{cut}}^{T(0,j)}$ ($f_{\mathrm{cut}}^{T(0,2)} = 40.62\,\mathrm{kHz}$, $f_{\mathrm{cut}}^{T(0,3)} = 71.85\,\mathrm{kHz}$, $f_{\mathrm{cut}}^{T(0,4)} = 103.31\,\mathrm{kHz}$ and $f_{\mathrm{cut}}^{T(0,5)} = 134.96\,\mathrm{kHz}$) and for increasing frequency their energy velocity increases, reaches a maximum and then decreases tending to the shear speed of the bitumen. Energy velocity maxima occur where the phase velocity dispersion curves of the $T(0,j)$ modes intersect the phase velocity curve of the $T_e(0,1)$ mode. In Fig. 3, the mode shape, the power flow density component $P_z^{T(0,2)}$ and the strain energy
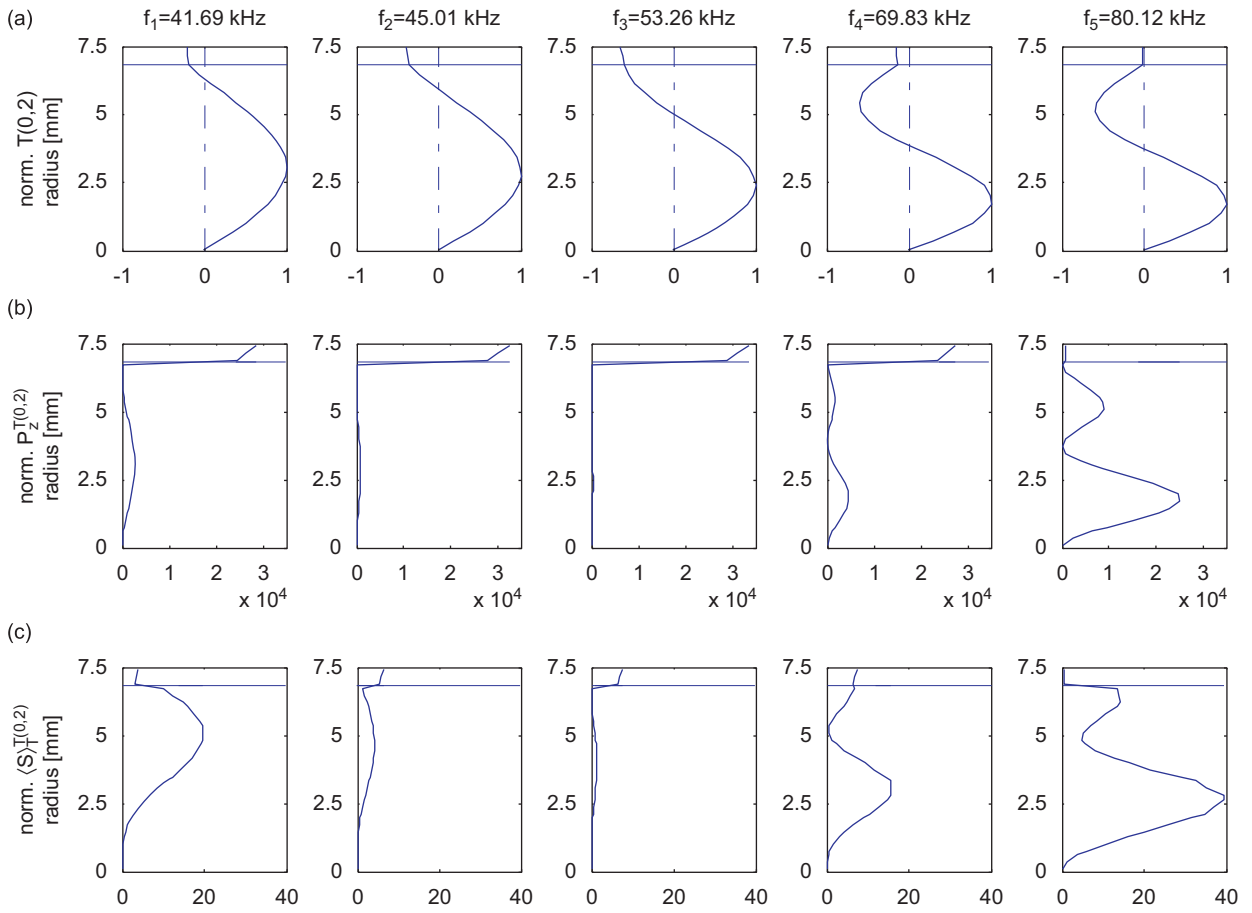
Fig. 3. $T(0,2)$ guided mode for a copper ($\rho = 8900 \, \text{kg m}^{-3}$, $c_T = 2240 \, \text{m s}^{-1}$, $\kappa_T = 0 \, \text{Np} \, \lambda^{-1}$) pipe, with inner radius 6.80 mm and wall thickness 0.70 mm, filled with elastic bitumen ($\rho = 970 \, \text{kg m}^{-3}$, $c_T = 430 \, \text{m s}^{-1}$, $\kappa_T = 0 \, \text{Np} \, \lambda^{-1}$) at different frequencies: (a) normalized mode shape; (b) normalized power flow density $P_z^{T(0,2)}$; (c) normalized strain energy density $\langle S^{T(0,2)} \rangle_T$. Frequency for each column is indicated at the top.

density $\langle S^{T(0,2)} \rangle_T$ for the $T(0,2)$ mode were calculated at five different frequencies to justify the energy velocity peaks.

The mode shapes were normalized with respect to their maximum value. The cross-sectional distributions of power flow density and strain energy density, calculated and represented within each element at the Gaussian points, were normalized by the mode power flow $\text{PF}^{T(0,2)}$ at the calculation frequency f_i. These normalizations were necessary in order to compare results at different frequencies.

From Fig. 3 it can be observed that at a frequency slightly bigger than the mode cut-off frequency, $f_1 = 41.69 \, \text{kHz}$, the $T(0,2)$ mode shows little motion in the tube wall and high strain energy density in the core. At around the cut-off frequency, in fact, the $T(0,2)$ mode corresponds to a standing wave across the thickness, and due to the large impedance difference between the core and the tube, the strain energy is mainly concentrated in the core.

As the frequency increases, ($f_2 = 45.01 \, \text{kHz}$), the amount of displacement and power flow in the tube wall slightly increases while the strain energy density decreases substantially.

At around $f_3 = 53.26 \, \text{kHz}$, where the $T(0,2)$ and $T_e(0,1)$ phase velocity curves intersect, most of the energy propagates in the tube rather than in the core where there is a minimum of strain energy density.

As the frequency increases further, displacement, power flow density and strain energy density in the pipe wall decrease, and for very high frequency they are primarily confined in the core. For example, at

$f_5 = 80.12$ kHz the $T(0,2)$ mode behaves as a shear wave in the core with phase and energy velocities close to the shear speed of the bitumen.

Therefore, according to Eq. (9) where the energy velocity is inversely proportional to the normalized energy density, the maximum of this feature must occur at around f_3 where the normalized strain energy is minimum. A similar behavior, not reported here, has been obtained for the Torsional $T(0,3)$, $T(0,4)$ and $T(0,5)$ modes at different frequency ranges.

When the bitumen core is considered as viscoelastic, Fig. 2(d–f), all the independent 23 Torsional modes $T_d(0,j)$ are damped (complex wavenumber). Among these solutions, only the $T_d(0,1)$ mode has attenuation smaller than 130 dB m^{-1}. This mode is generated by the coupling of the formerly undamped modes branch due to the bitumen viscosity. Similar branch connection phenomena were observed in viscoelastic orthotropic and isotropic plates [21,22]. This mode starts propagating at around 2029.2 m/s phase speed. At increasing frequency its velocity tends to the bulk shear speed of the copper as an opposite to the undamped $T(0,i)$ modes that were tending to the shear bulk wave speed of the bitumen.

The higher $T_d(0,j)$ $j = 2,3,\ldots,23$ modes propagate in the 0–150 kHz frequency range with non-zero phase and energy velocity, and extend to the origin of the frequency axis at zero value. Each higher $T_d(0,j)$ mode, below the $f_{cut}^{T(0,i)}$ cut-off frequencies of the equivalent undamped mode $T(0,j)$, is characterized by attenuation values (Fig. 2(f)) close to the one of the evanescent modes of the undamped case (Fig. 2(c)), and very small energy velocity. Around the $f_{cut}^{T(0,i)}$ cut-off frequency, the attenuation of the damped mode reaches a minimum and the energy velocity starts to increase. For increasing frequency, the mode attenuation grows linearly while the energy velocity remains constant (see Fig. 2(e) and (f)).
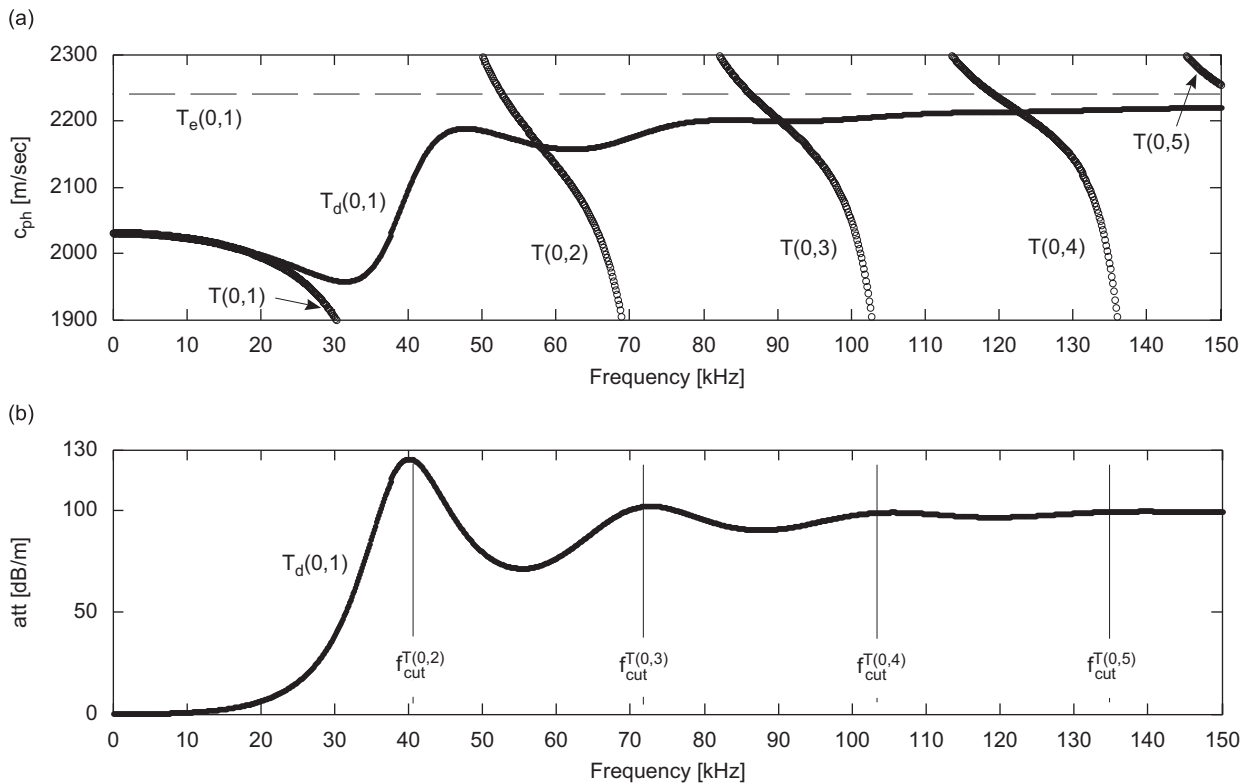
(a)

(b)

Fig. 4. Torsional $T_d(0,1)$ mode phase velocity (a) and attenuation (b) dispersion curves (●●●●) for a copper ($\rho = 8900$ kg m^{-3}, $c_T = 2240$ m s^{-1}, $\kappa_T = 0$ Np λ^{-1}) pipe, with inner radius 6.80 mm and wall thickness 0.70 mm, filled with viscoelastic bitumen ($\rho = 970$ kg m^{-3}, $c_T = 430$ m s^{-1}, $\kappa_T = 1.35$ Np λ^{-1}). Also shown in (a) the dispersion curves (○○○○) for the $T(0,i)$ modes of the equivalent undamped system. The dashed line corresponds to the non-dispersive fundamental Torsional mode for the empty copper pipe $T_e(0,1)$.

In Fig. 4 dispersion results for the undamped and damped systems are overlapped and represented in the 1900–2300 m s^{-1} phase speed range, Fig. 4(a), and in the 0–130 dB m^{-1} attenuation range, Fig. 4(b). Modes with attenuation larger than 130 dB m^{-1} are not shown. It can be noted that the behavior of the $T_d(0,1)$ mode is in perfect agreement with the results proposed by Simonetti and Cawley [34], proving the reliability of the proposed SAFE damped formulation.

Local maxima in the $T_d(0,1)$ attenuation spectrum occur around the mode cut-off frequencies of the undamped system. Interestingly, the minima of $T_d(0,1)$ attenuation occur for those frequencies where the phase velocity curves of $T(0,j)$ and $T_e(0,1)$ mode intersect.

It is well known that in undamped waveguides the Poynting vector is parallel to the z-axis while for damped media a non-zero radial component P_r^m appears. In the following, the link between P_r^m and mode attenuation is analyzed.

In Fig. 5(a) the $P_r^{T_d(0,1)}$ component integrated over the waveguide cross-section Ω and normalized with respect to the mode power flow $PF^{T_d(0,1)}$ is represented. It can be noted that this ratio presents a similar behavior to the $T_d(0,1)$ mode attenuation shown in Fig. 4(b). In Fig. 5(b) and (c), are represented the normalized $T_d(0,1)$ mode shapes and cross-sectional distributions of the radial power flow density, respectively.
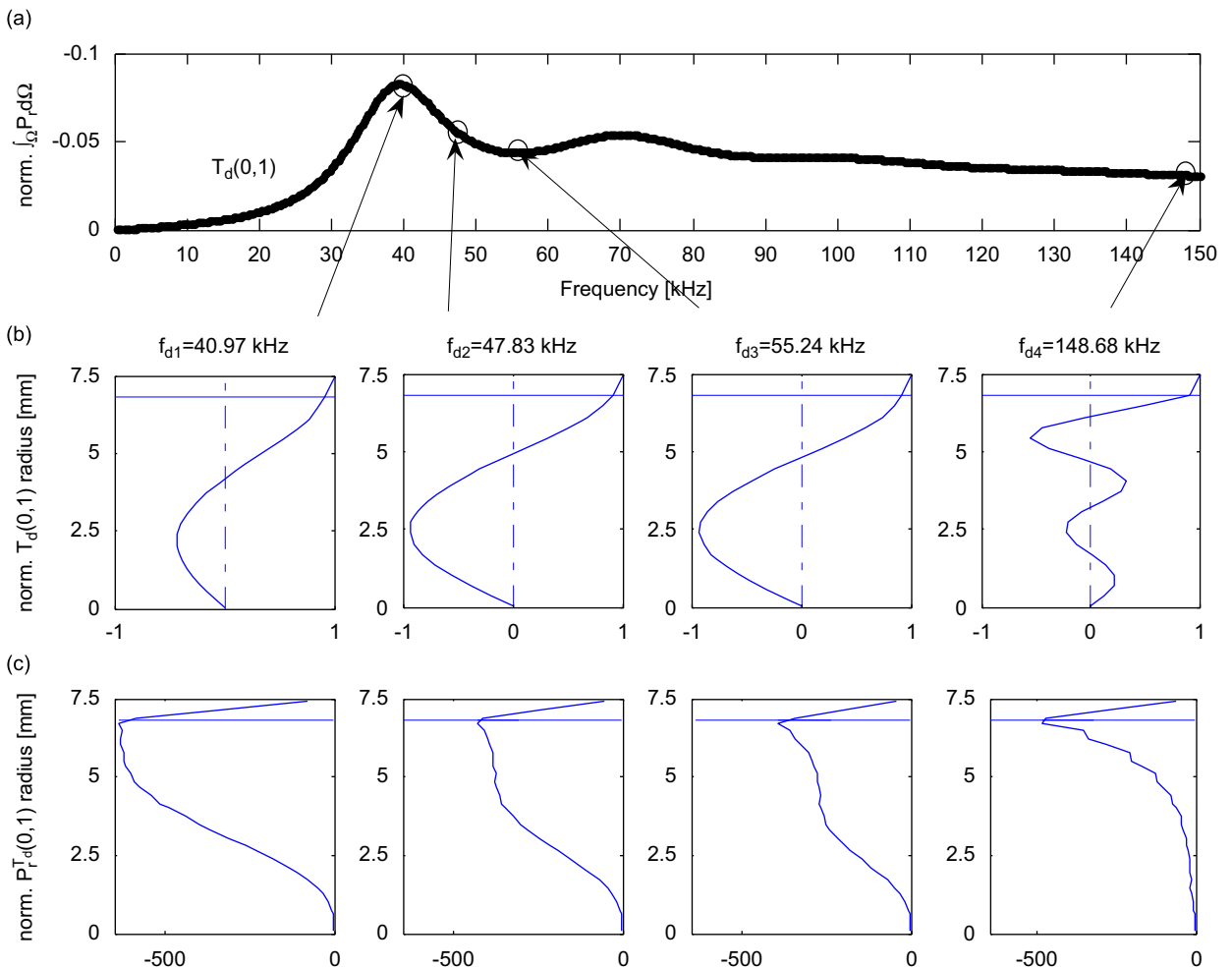

Fig. 5. Torsional $T_d(0,1)$ mode for a copper ($\rho = 8900 \, \text{kg m}^{-3}$, $c_T = 2240 \, \text{m s}^{-1}$, $\kappa_T = 0 \, \text{Np} \, \lambda^{-1}$) pipe with inner radius 6.80 mm and wall thickness 0.70 mm filled with viscoelastic bitumen ($\rho = 970 \, \text{kg m}^{-3}$, $c_T = 430 \, \text{m s}^{-1}$, $\kappa_T = 1.30 \, \text{Np} \, \lambda^{-1}$). (a) Normalized radial power flow density $P_r^{T_d(0,1)}$ integrated over the waveguide cross-section Ω. (b) Normalized mode shape. (c) Normalized radial power flow density $P_r^{T_d(0,1)}$. Frequency for each column is indicated at the top.

At $f_{d1} = 40.97$ kHz, where the $T_d(0,1)$ mode shows an attenuation peak, the normalized cross-sectional distribution of the radial power flow density is maximum. In contrast at $f_{d3} = 55.24$ kHz where a local minimum of the normalized radial power flow takes place, the $T_d(0,1)$ mode attenuation minimum occurs.

5.2. Elastic steel pipe coated by a thin layer of viscoelastic bitumen

An elastic scheduled 4-in ANSI 40 steel pipe coated with a thin layer of viscoelastic bitumen was chosen because it was studied in depth by Barshinger et al. [31,32]. In these references phase velocity and attenuation dispersion curves for the Longitudinal modes with $att^{(m)} < 10$ dB m^{-1} were obtained by using a SPBW-based formulation. Waveguide geometric and acoustic properties are given in Table 1. The bulk wave attenuations for the viscoelastic bitumen were calculated as $\kappa_{L,S} = 2\pi c_{L,S}(\alpha_{L,S}/\omega)$, where $\alpha_{L,S}/\omega$ is given in Ref. [32].

According to the mesh criterion of Ref. [40] twelve finite elements across the steel pipe thickness and three elements for the bitumen layer were used. For the Longitudinal modes, only the 62 u_r and u_z dof of the total $[n_{el} \times (n_n - 1) + 1] \times n_{dof} = 93$ dof were used ($n_{el} = 15$) to formulate the wave equation.

In Fig. 6 SAFE results in terms of phase velocity, energy velocity and attenuation dispersion curves are shown in the 0–1 MHz frequency range. The results are in excellent agreement with those proposed in both Refs. [31,32]. Here, in addition, the roots with $att^{(m)} > 10$ dB m^{-1} are represented with a brighter color.

In the examined frequency range, among the independent 62 complex roots, the number of damped modes with $att^{(m)} < 10$ dB m^{-1} range from 1 to 5 for increasing frequency. The phase and energy velocity dispersion curve of these modes look quite similar to the phase and group velocity dispersion curves of an elastic 4-in 40 ANSI steel pipe. This is due to the fact that the bitumen coating is very thin in comparison with the elastic pipe layer.
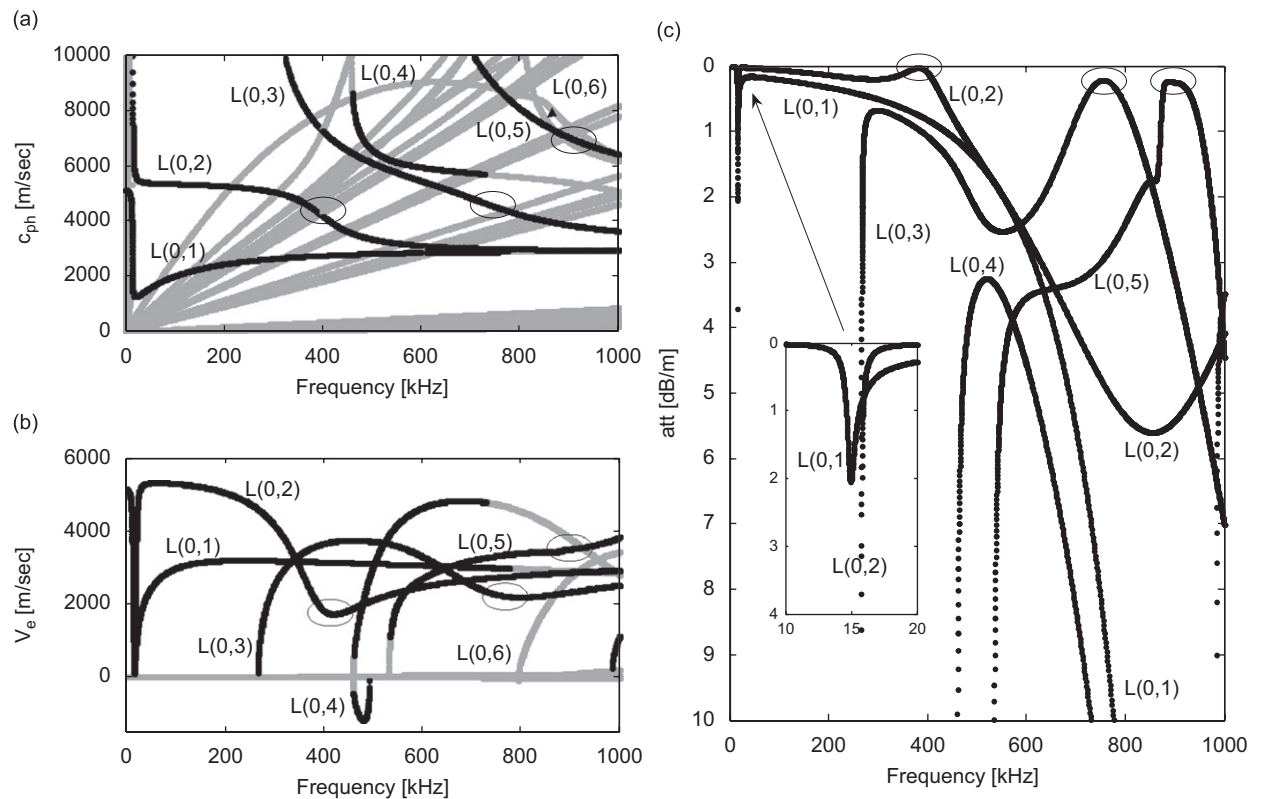

Fig. 6. Longitudinal modes for an elastic ($\rho = 7800$ kg m^{-3}, $c_L = 5900$ m s^{-1}, $c_T = 3190$ m s^{-1}) 4-in scheduled ANSI 40 steel pipe coated with 0.1524 mm of viscoelastic bitumen ($\rho = 1500$ kg m^{-3}, $c_L = 1860$ m s^{-1}, $c_T = 750$ m s^{-1}, $\kappa_L = 0.2688$ Np λ^{-1}, $\kappa_T = 1.1310$ Np λ^{-1}) examined in Ref. [32]. (a) Phase velocity, (b) energy velocity and (c) attenuation curves. Low attenuation points are highlighted with an ellipse.

In Fig. 6(c) it is interesting to note a high dispersive behavior of the attenuation curves. In this plot, three frequency-mode combinations with particularly low attenuation values are highlighted with an ellipse. These combinations have great potential for performing NDE tests in coated pipes as demonstrated experimentally in Ref. [31].

From the energy velocity dispersion curves, Fig. 6(b), it can be noted that the $L(0,4)$ mode exists also as a "backwards" wave where its phase and energy velocity have opposite signs. The attenuation of this "backwards" wave has negative values and it is not represented in Fig. 6(c).

Also for this second example, it can be seen in Fig. 7(a) that the radial power flow $P_r{}^{L(0,i)}$ integrated over the waveguide cross-section and normalized with respect to the modes power flow $PF^{L(0,i)}$ look like the dispersive GUWs attenuation curves of Fig. 6(c). In Fig. 7(b) and (c) the normalized mode shapes and the normalized cross-sectional distribution of the radial power flow density are represented at three different frequencies.

At $f_2 = 749.69\,\text{kHz}$, where the $L(0,3)$ attenuation curve has a minimum, both the u_z displacement component in the bitumen layer and the radial power flow distribution have a very small magnitude. These features, have larger values at f_1 and f_3.

Some minor differences can be noted by comparing the SPBW results in Refs. [31,32] and the SAFE results of Fig. 6. In Ref. [31] some solutions of the attenuation curves are missing resulting in interrupted or discontinuous branches. The SAFE results show no missing roots. Furthermore, in Ref. [31] the attenuation
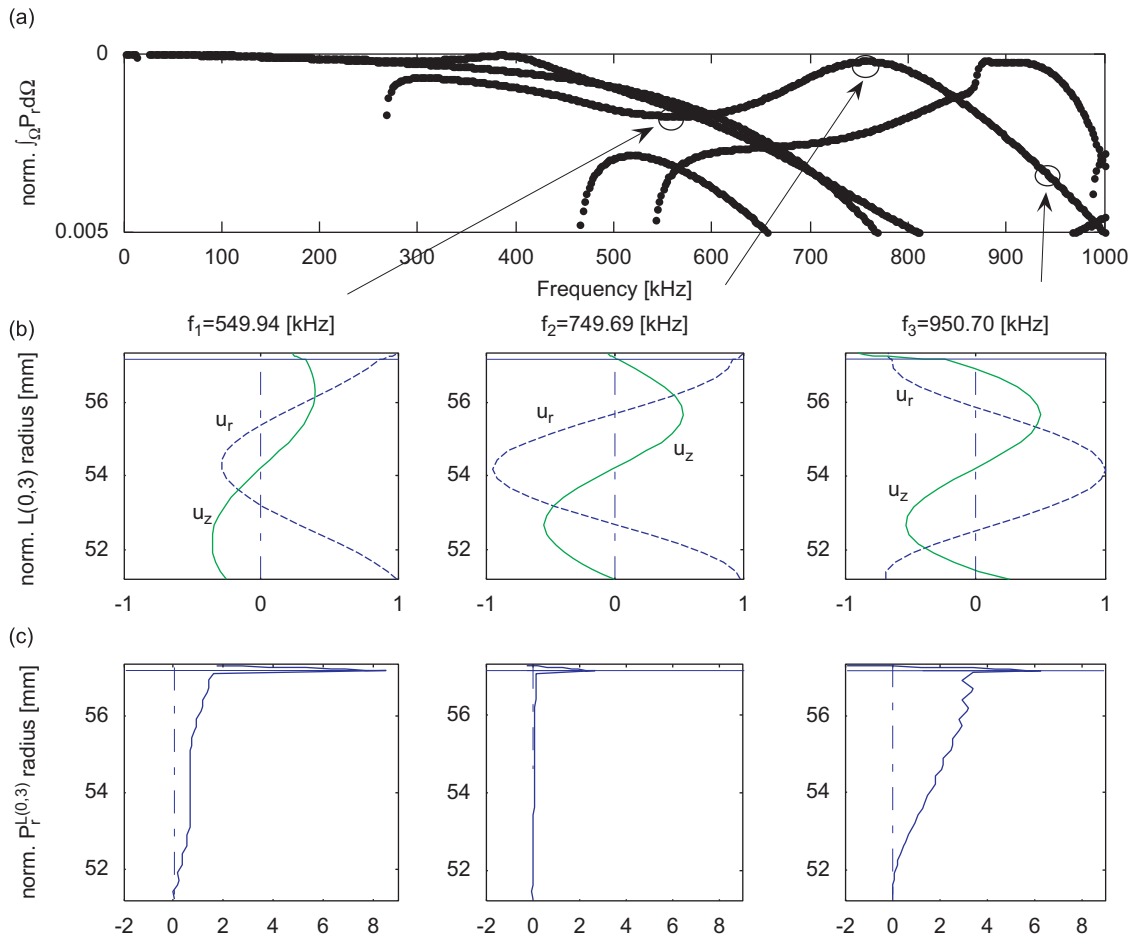

Fig. 7. Longitudinal modes for an elastic ($\rho = 7800\,\text{kg m}^{-3}$, $c_L = 5900\,\text{m s}^{-1}$, $c_T = 3190\,\text{m s}^{-1}$) 4-in scheduled ANSI 40 steel pipe coated with $0.1524\,\text{mm}$ of viscoelastic bitumen ($\rho = 1500\,\text{kg m}^{-3}$, $c_L = 1860\,\text{m s}^{-1}$, $c_T = 750\,\text{m s}^{-1}$, $\kappa_L = 0.2688\,\text{Np}\,\lambda^{-1}$, $\kappa_T = 1.1310\,\text{Np}\,\lambda^{-1}$) examined in Ref. [32]. (a) Normalized radial power flow density $P_r{}^{L(0,i)}$ integrated over the waveguide cross-section Ω. (b) Normalized $L(0,3)$ mode shapes. (c) Normalized $L(0,3)$ radial power flow density $P_r{}^{L(0,3)}$. Frequency for each column is indicated at the top.

for both $L(0,1)$ and $L(0,2)$ modes grows exponentially at around the $L(0,2)$ mode cut-off frequency for the equivalent undamped system ($f_{cut}^{L(0,2)} = 15.74$ kHz), while in the SAFE results the $L(0,1)$ attenuation branch extends to the origin of the frequency axis (see the inset in Fig. 6(c)). This behavior is expected since the fundamental modes must have zero attenuation at zero frequency.

5.3. Viscoelastic steel strand embedded in post-tensioned concrete structures

Steel strands embedded in grout provide the necessary level of prestress in post-tensioned concrete structures. Studying GUW propagation in these components is important to design effective NDE methods for detecting defects and monitoring loads [25]. The aim of this SAFE simulation is to identify the modes which have low attenuation as they propagate along the strand-grout-concrete waveguide (see Fig. 8) in order to maximize the inspection coverage.

In this example the waveguide consists of a 15.24 mm-diameter viscoelastic steel bar embedded in a 63.50 mm outer diameter duct, completely full of viscoelastic grout, surrounded by a layer of concrete with external diameter equal to 152.40 mm. The present three-layer axial symmetric waveguide models the prestressed concrete specimen represented in Fig. 8(a) and (b) which was the subject of several experimental tests reported elsewhere [40]. The waveguide geometrical and acoustic properties are given in Table 1.

For a maximum frequency $f_{max} = 700$ kHz, the mesh criteria proposed in Ref. [40] required 7 finite elements in the steel bar, 40 elements in the grout layer and 58 elements in the concrete layer. Only the 422 dof in the radial and axial direction were used for the representation of the Longitudinal $L(0,i)$ modes.

Fig. 9 shows the SAFE dispersion results for the Longitudinal modes in terms of phase velocity (a), energy velocity (b) and attenuation (c). Roots with attenuation larger than 100 dB m^{-1} are marked with a brighter color. The dispersion curves look quite complex if compared to the ones of the previous examples. In this case, in fact, 422 damped roots are obtained at each frequency with the adopted mesh. However, some frequency-mode combination with low attenuation can be easily found.

For example, highlighted in the insets of Fig. 9 are the three low attenuated modes ($\bullet$, $\blacktriangledown$, $\blacksquare$) at 305 kHz:

- $\bullet$　att $= 51.3$ dB m^{-1}, $c_{ph} = 3323.3$ m s^{-1}, $Ve = 2408.6$ m s^{-1};
- $\blacktriangledown$　att $= 59.3$ dB m^{-1}, $c_{ph} = 2855.1$ m s^{-1}, $Ve = 2488.2$ m s^{-1};
- $\blacksquare$　att $= 61.7$ dB m^{-1}, $c_{ph} = 3079.2$ m s^{-1}, $Ve = 2269.4$ m s^{-1}.
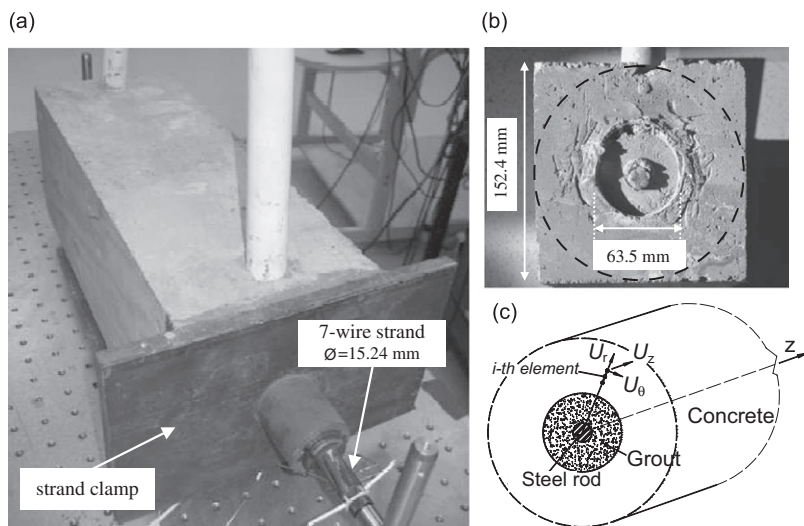

Fig. 8. (a) Seven wire strand embedded in grout and concrete block. (b) Section of the specimen. (c) Three layer system considered in the SAFE model.
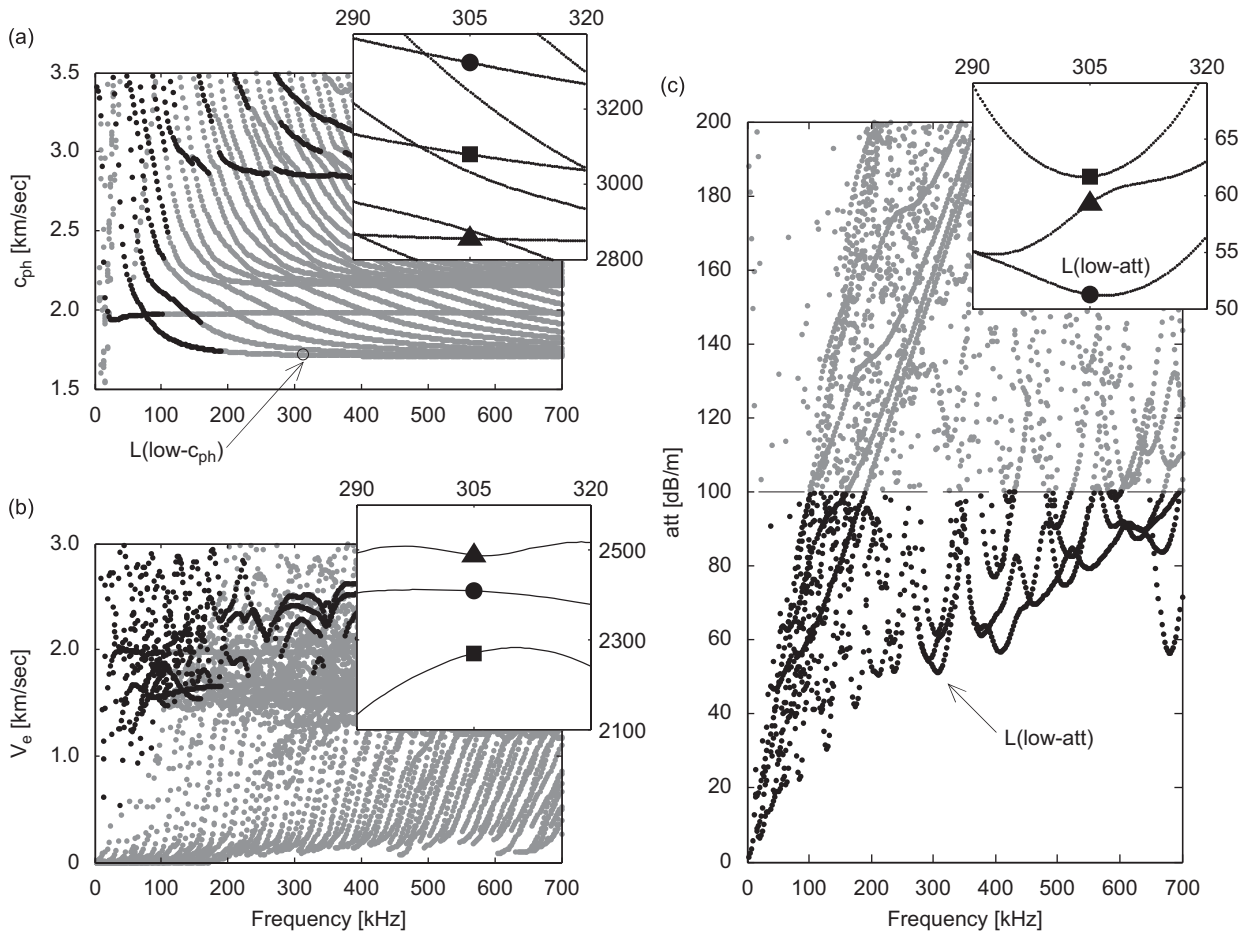
Fig. 9. Phase velocity (a), energy velocity (b) and attenuation (c) dispersion curves for the longitudinal $L(0,i)$ guided modes in a three-layer waveguide: viscoelastic steel bar ($\varnothing = 15.24$ mm, $\rho = 7932$ kg m^{-3}, $c_L = 5960$ m s^{-1}, $c_T = 3260$ m s^{-1}, $\kappa_L = 0.003$ Np λ^{-1}, $\kappa_T = 0.008$ Np λ^{-1}) embedded in a viscoelastic layer of grout ($\varnothing = 63.50$ mm, $\rho = 1600$ kg m^{-3}, $c_L = 2810$ m s^{-1}, $c_T = 1700$ m s^{-1}, $\kappa_L = 0.043$ Np λ^{-1}, $\kappa_T = 0.100$ Np λ^{-1}) and a viscoelastic layer of concrete ($\varnothing = 152.40$ mm, $\rho = 2200$ kg m^{-3}, $c_L = 3900$ m s^{-1}, $c_T = 2200$ m s^{-1}, $\kappa_L = 0.200$ Np λ^{-1}, $\kappa_T = 0.400$ Np λ^{-1}). Three low attenuated modes at 305 kHz are highlighted in the insets.

It can be seen that at around 305 kHz these modes have a maximum of energy velocity. This property is useful to limit the effect of pulse dispersion and to reduce the risk of mode overlapping that generally complicates the measurements. With low attenuation and low dispersive energy velocity, these modes are good candidates for NDE of this system.

The mode with smallest attenuation (●) is also labeled as $L(0,\text{low-att})$ in Fig. 9(c), while the mode with lowest phase speed at 305 kHz is highlighted $L(0,\text{low-}c_{\text{ph}})$ in Fig. 9(a). The $L(0,\text{low-}c_{\text{ph}})$ mode has a phase speed $c_{ph} = 1713.6$ m s^{-1}, attenuation equal to 157.9 dB m^{-1} and energy velocity $Ve = 1685.3$ m s^{-1}.

Fig. 10 presents the normalized mode shapes, the normalized radial and axial power flow distribution, as well as the normalized strain energy density for the $L(0,\text{low-}c_{ph})$ and $L(0,\text{low-att})$ modes at 305 kHz. It can be seen that the $L(0,\text{low-}c_{ph})$ mode displacement, Fig. 10(a), is mainly in the radial direction with very little displacement in the axial direction. Radial power flow and energies are confined to the grout layer. As a result, the mode behaves as a shear wave traveling at a speed close to the shear bulk speed of the grout. From Fig. 10(b), it can be noted that the $L(0,\text{low-att})$ displacements are concentrated within the steel rod and the grout layer. The radial power flow is distributed between the steel and the grout with a transmission peak at the interface. The energy for this mode is mainly flowing in the strand while only a small amount is present in the grout. Therefore, traveling mainly in the less attenuating media, the mode has small attenuation at this particular frequency.
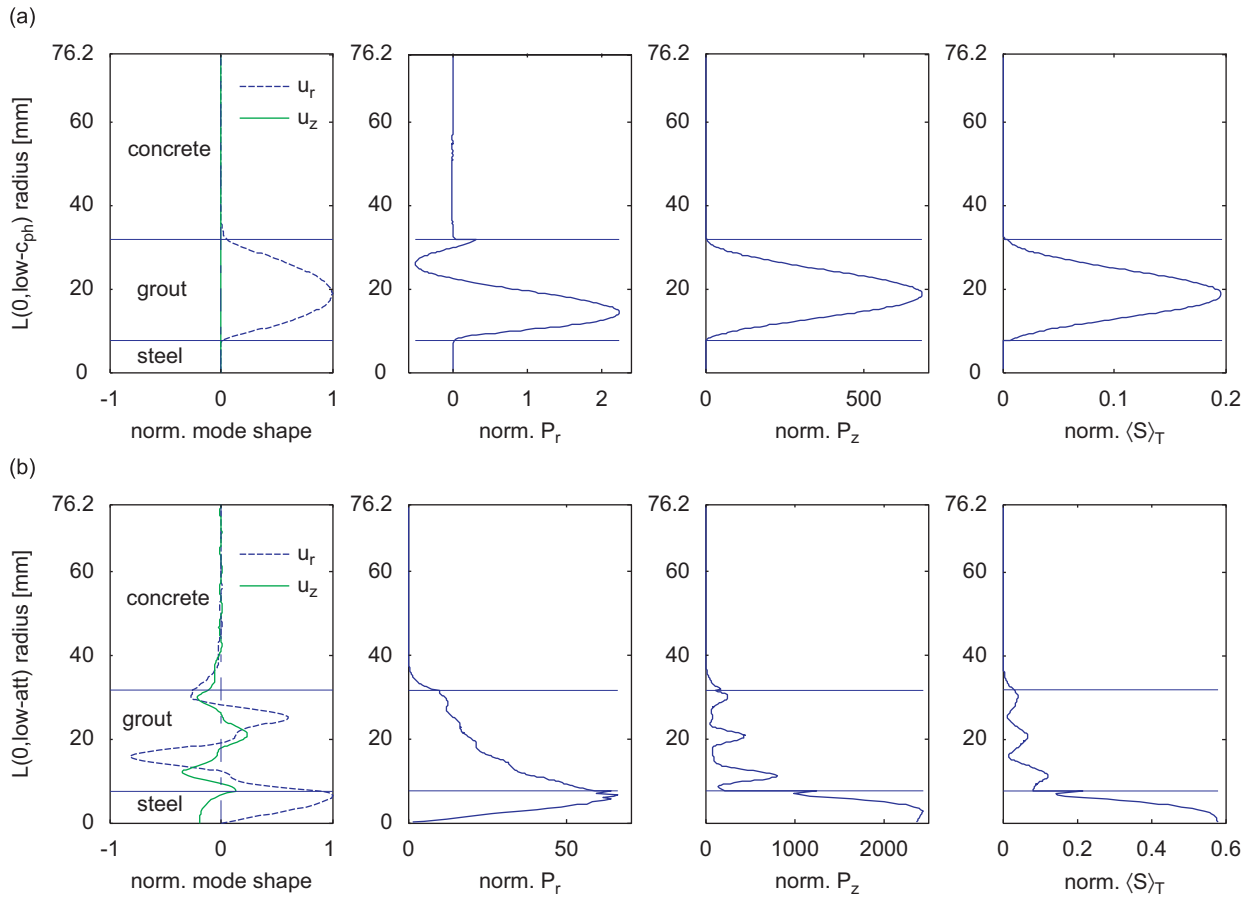
Fig. 10. (a) Lowest phase velocity longitudinal mode $L(0,\text{low-}c_{ph})$ and (b) lowest attenuation longitudinal mode $L(0,\text{low-}att)$ in the three-layer steel-grout-concrete viscoelastic waveguide at 305 kHz. First column: normalized mode shape. Second column: normalized radial power flow density $P_r^{L(0,i)}$. Third column: normalized axial power flow density $P_z^{L(0,i)}$. Fourth column: normalized strain energy density $\langle S^{L(0,i)} \rangle_T$.

This kind of analysis can help designing an NDE system that makes use of guided modes with ultrasonic energy mainly concentrated within the strand.

While SAFE computational time to obtain the results of the first and second examples is negligible, on the order of a few seconds, it should be noted that the larger mesh adopted in the current example results in a significant calculation time. The analysis carried out on a 2.6 GHz Pentium 4 processor with 1 GB of RAM typically employs 100–120 min in this case. The increase in the computational cost is mainly related to the solution of the eigenvalue problems.

6. Conclusions

This paper proposes a SAFE formulation for modeling ultrasonic guided wave in axysimmetric waveguides. The novelty over general SAFEs formulations is the possibility to model waveguides with material damping. Damping is included at the element level by accounting for linear viscoelastic materials in force of the correspondence principle.

The proposed SAFE formulation was successful in replicating the results of SPBW methods in layered damped systems. Specific advantages of the damped SAFE algorithm compared to SPBW methods are: (i) the complex roots are obtained with standard routines for eigenvalue problems that show no missing roots; (ii) the formulation does not result in any instability for the bulk velocities of the materials, (iii) the "mode tracing"

problem is avoided since the energy velocity is obtained without considering adjacent solutions, (iv) different rheological models can be easily accounted for viscoelastic materials without the need for reformulating the governing equations.

Despite the advantages of the proposed SAFE formulation in modeling ultrasonic guided waves in damped waveguides, an interested reader should be aware of the current limitations of the technique: (i) the development of a SAFE formulation is limited to users with sufficient familiarity with Finite Element analysis; (ii) the accuracy of the SAFE method is frequency and mesh dependent, where large meshes can lead to computationally expensive eigenvalue problems; (iii) while SPBW-based formulations can account for attenuation induced by wave energy leakage in a surrounding semi-medium current, SAFE frameworks cannot accurately capture this source of energy dissipation until absorbing or infinite elements are successfully implemented at the outer boundaries of the structure.

Acknowledgments

References

[1] D.E. Muller, A method for solving algebraic equations using an automatic computer, *Mathematical Tables and Aids to Computation* 10 (1956) 208–215.
[2] M.J.S. Lowe, Matrix techniques for modeling ultrasonic waves in multilayered media, *IEEE Transactions on Ultrasonics, Ferroelectrics, and Frequency Control* 42 (1995) 525–542.
[3] K.P. Soldatos, Review of three dimensional dynamic analyses of circular cylinders and cylindrical shells, *ASME Journal of the Applies Mechanics Review* 47 (10) (1994) 501–516.
[4] R.B. Nelson, S.B. Dong, R.D. Kalra, Vibrations and waves in laminated orthotropic circular cylinders, *Journal of Sound and Vibration* 18 (3) (1971) 429–444.
[5] S.B. Dong, R.B. Nelson, On natural vibrations and waves in laminated orthotropic plates, *Journal of Applied Mechanics* 39 (3) (1972) 739–745.
[6] B. Aalami, Waves in prismatic guides of arbitrary cross section, *Journal of Applied Mechanics* 40 (1973) 1067–1072.
[7] K.H. Huang, S.B. Dong, Propagating waves and edge vibrations in anisotropic composite cylinders, *Journal of Sound and Vibration* 96 (3) (1984) 363–379.
[8] P.C. Xu, S.K. Datta, Characterization of fiber–matrix interface by guided waves: axisymmetric case, *Journal of the Acoustical Society of America* 89 (6) (1991) 2573–2583.
[9] N. Rattanawangcharoen, A.H. Shah, S.K. Datta, Wave propagation in laminated composite circular cylinders, *International Journal of Solids and Structures* 29 (1992) 767–781.
[10] S.B. Dong, K.H. Huang, Edge vibrations in laminated composite plates, *Journal of Applied Mechanics* 41 (1985) 322–327.
[11] S.K. Datta, A.H. Shah, R.L. Bratton, T. Chakraborty, Wave propagations in laminated composite plates, *Journal of the Acoustical Society of America* 83 (6) (1988) 2020–2026.
[12] O.M. Mukdadi, Y.M. Desai, S.K. Datta, A.H. Shah, A.J. Niklasson, Elastic guided waves in a layered plate with rectangular cross section, *Journal of the Acoustical Society of America* 112 (2002) 1766–1779.
[13] A.C. Hladky-Hennion, Finite element analysis of the propagation of acoustic waves in waveguides, *Journal of Sound and Vibration* 194 (2) (1996) 119–136.
[14] L. Gavrić, Computation of propagative waves in free rail using a finite element technique, *Journal of Sound and Vibration* 185 (3) (1995) 531–543.
[15] T. Hayashi, W.J. Song, J.L. Rose, Guided wave dispersion curves for a bar with an arbitrary cross-section, a rod and rail example, *Ultrasonics* 41 (2003) 175–183.
[16] X. Han, G.R. Liu, Z.C. Xi, K.Y. Lam, Characteristics of waves in a functionally graded cylinder, *International Journal for Numerical Methods in Engineering* 53 (2002) 653–676.
[17] G.R. Liu, K.Y. Dai, X. Han, T. Ohyoshi, Dispersion of waves and characteristic wave surfaces in functionally graded piezoelectric plates, *Journal of Sound and Vibration* 268 (1) (2003) 131–147.
[18] E. Taciroglu, C.W. Liu, S.B. Dong, C.K. Chun, Analysis of laminated piezoelectric circular cylinders under axisymmetric mechanical and electrical loads with a semi-analytic finite element method, *International Journal of Solids and Structures* 41 (2004) 5185–5208.
[19] S. Finnveden, Evaluation of modal density and group velocity by a finite element method, *Journal of Sound and Vibration* 273 (2004) 51–75.

[20] P.J. Shorter, Wave propagation and damping in linear viscoelastic laminates, *Journal of the Acoustical Society of America* 115 (2004) 1917–1925.

[21] I. Bartoli, A. Marzani, F. Lanza di Scalea, E. Viola, Modeling wave propagation in damped waveguides of arbitrary cross-section, *Journal of Sound and Vibration* 295 (3–5) (2006) 685–707.

[22] A. Bernard, M.J.S. Lowe, M. Deschamps, Guided waves energy velocity in absorbing and non-absorbing plates, *Journal of the Acoustical Society of America* 110 (2001) 186–196.

[23] G. Neau, M.J.S. Lowe, M. Deschamps, Propagation of lamb waves in anisotropic and absorbing plates: theoretical derivation and experiments, *Review of Progress in Quantitative NDE* 21 (2002) 1062–1069.

[24] G. Neau, Lamb Waves in Anisotropic Viscoelastic Plates. Study of the Wave Fronts and Attenuation. Ph.D. Thesis, L'Université Bordeux I, Bordeux, 2003.

[25] B.N. Pavlakovic, M.J.S. Lowe, P. Cawley, High-frequency low-loss ultrasonic modes in imbedded bars, *Journal of Applied Mechanics* 68 (2001) 67–75.

[26] H. Matt, I. Bartoli, F. Lanza di Scalea, Ultrasonic guided wave monitoring of composite wing skin-to-spar bonded joints in aerospace structures, *Journal of the Acoustic Society of America* 118 (2005) 2240–2252.

[27] F. Lanza di Scalea, H. Matt, I. Bartoli, S. Coccia, G. Park, C.R. Farrar, Health Monitoring of UAV Wing Skin-to-spar Joints using Guided Waves and Macro Fiber Composite Transducers, *Journal of Intelligent Material Systems and Structures* (2006).

[28] R.M. Christensen, *Theory of Viscoelasticity: An Introduction*, second ed., Academic Press, New York, 1982.

[29] W. Zhuang, A.H. Shah, S.B. Dong, Elastodynamic Green's function for laminated anisotropic circular cylinders, *Journal of Applied Mechanics* 66 (3) (1999) 665–674.

[30] J.L. Rose, *Ultrasonic Waves in Solid Media*, Cambridge University Press, Cambridge, 1999.

[31] J. Barshinger, J.L. Rose, M.J. Avioli Jr., Guided wave resonance tuning for pipe inspection, *Journal of Pressure Vessel Technology* 124 (2002) 303–310.

[32] J. Barshinger, J.L. Rose, Guided wave propagation in an elastic hollow cylinder coated with a viscoelastic material, *IEEE Transactions on Ultrasonics, Ferroelectrics, and Frequency Control* 51 (11) (2004) 1547–1556.

[33] E. Pan, J. Rogers, S.K. Datta, A.H. Shah, Mode selection of guided waves for ultrasonic inspection of gas pipelines with thick coating, *Mechanics of Materials* 31 (1999) 165–174.

[34] F. Simonetti, P. Cawley, A guided wave technique for the characterization of highly attenuative viscoelastic materials, *Journal of the Acoustical Society of America* 114 (1) (2003) 158–165.

[35] B.N. Pavlakovic, M.J.S. Lowe, D.N. Alleyne, P. Cawley, Disperse: a general purpose program for creating dispersion curves, in: D.O. Thompson, D.E. Chimenti (Eds.), *Review of Progress in Quantitative NDE*, Vol. 16, Plenum, New York, 1997, pp. 185–192.

[36] M.A. Biot, General theorems on the equivalence of group velocity and energy transport, *The Physical Review* 105 (4) (1957) 1129–1137.

[37] J.D. Achenbach, *Wave Propagation in Elastic Solids*, North-Holland, 1973.

[38] B.A. Auld, *Acoustic Fields and Waves in Solids (two volumes)*, Krieger Publishing Company, Malabar, FL, 1990.

[39] F. Seco, J.M. Martín, A.R. Jiménez, J.L. Pons, L. Calderón, R. Ceres, PCDISP: a tool for the simulation of wave propagation in cylindrical waveguides, *Proceedings of the Ninth International Congress on Sound and Vibration*, Orlando, FL, 2002.

[40] J.M. Galan, R. Abascal, Numerical simulation of Lamb wave scattering in semi-finite plates, *International Journal for Numerical Methods in Engineering* 53 (2002) 1145–1173.

[41] I. Bartoli, A. Marzani, F. Lanza di Scalea, P. Rizzo, E. Viola, E. Sorrivi, R. Phillips, SAFE modeling of waves for the structural health monitoring of prestressing tendons, *Proceedings of SPIE's 14th Annual International Symposium on Smart Structures and Materials*, 65320D, 2007.